

Compressed Intermetallic PdCu for Enhanced Electrocatalysis

Michelle M. Flores Espinosa, Tao Cheng, Mingjie Xu, Luca Abatemarco, Chungseok Choi, Xiaoqing Pan, William A. Goddard, III, Zipeng Zhao,* and Yu Huang*



Cite This: *ACS Energy Lett.* 2020, 5, 3672–3680



Read Online

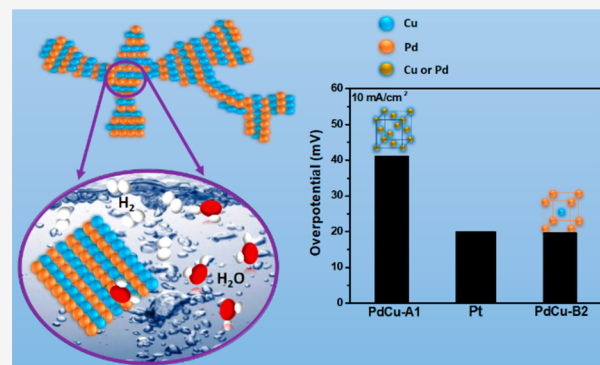
ACCESS |

Metrics & More

Article Recommendations

Supporting Information

ABSTRACT: Hydrogen evolution reaction (HER) is a key reaction in hydrogen production through water electrolysis. Platinum (Pt) is the best-known element for HER catalysis. Due to the scarcity of Pt, the development of non-Pt nanocatalysts is desired to achieve broad scale implementations. Here we demonstrate that the PdCu nanostructure containing an intermetallic B2 phase (PdCu-B2) shows a smaller Tafel slope, higher exchange current density, and lower overpotential for HER compared to commercial Pt/C in acidic conditions. Density functional theory (DFT) calculations demonstrate that the improved HER performance in acidic conditions can be attributed to the decrease in the hydrogen binding energy (HBE) on the compressed intermetallic PdCu-B2, shifting the HBE to a more optimal position even compared to Pt/C. In addition, PdCu-B2 exhibits the highest mass activity toward the formic acid oxidation reaction, making it a good anode catalyst candidate for formic-acid-based fuel cells.



The migration from fossil-fuel-based energy supplies to renewable energies with low pollutant emissions is imperative for a sustainable environment. Hydrogen is globally known as a future green fuel source, leading to zero carbon dioxide emissions.¹ Hydrogen (H_2) generation can be accomplished by natural gas reforming or electrochemical water (H_2O) splitting at an applied potential (U) in the presence of an electrocatalyst.^{2–5} The hydrogen evolution reaction (HER), the cathodic reaction in electrochemical water splitting, is accompanied by adsorption of hydrogen (*H) on the electrode surface and its reaction with H_2O to form H_2 . To enhance the HER kinetics, the catalyst must induce proton reduction with minimal overpotential (η), high current densities, and high faradaic efficiency while exhibiting fast kinetics.^{5,6} Pt-based materials are optimal catalysts for HER.⁷ Nevertheless, the cost and scarcity of Pt makes Pt-based catalysts unsuitable for large scale applications.^{8,9}

Pd-based materials and alloys with transition metals (e.g., Cu, Ag, Ni, Co, Fe, Ru) are attractive candidates due to their similar chemical stability to that of noble metals but at higher abundance than Pt.^{8,10–20} Pd and Pd alloy nanoparticles (NPs) have been widely studied due to their high surface area, but they usually suffer from agglomeration.^{10,21} One dimensional (1D) nanomaterials, on the other hand, suffer from far less agglomeration.^{9,22,23} The interconnected nature of 1D nanomaterials significantly increases the electrical conductivity to

enhance the activity and structure stability compared with NPs.^{10,24} Meanwhile, intermetallic compounds with high atomic ordering have been shown to demonstrate multifunctional catalytic activities and better stability over random alloy materials.^{18,25–31} Nevertheless, these intermetallic compounds are often obtained at high annealing temperatures^{30,31} to overcome the activation energy barrier for interdiffusion and the subsequent equilibrium of atoms toward a more ordered structure which ultimately induces Ostwald ripening, reducing the surface area to volume ratio. For example, Pt_3Co and Pd_3Pb intermetallic nanowires (NWs) showed improved activities toward reduction and oxidation reactions compared with their alloy counterparts despite displaying relatively low electrochemical active surface areas (ECSAs) of around 52.1 and $44.8\text{ m}^2/\text{g}$, respectively.^{32,33} In addition, alloying Pd with CO poison resistant transition metal hosts^{16–18,34} has been reported to be effective catalyst within fuel cell systems,^{16,35,36} such as the formic acid oxidation reaction (FAOR) which is the anodic reaction in direct formic acid fuel cells (DFAFCs),

Received: September 14, 2020

Accepted: October 26, 2020

Published: November 3, 2020



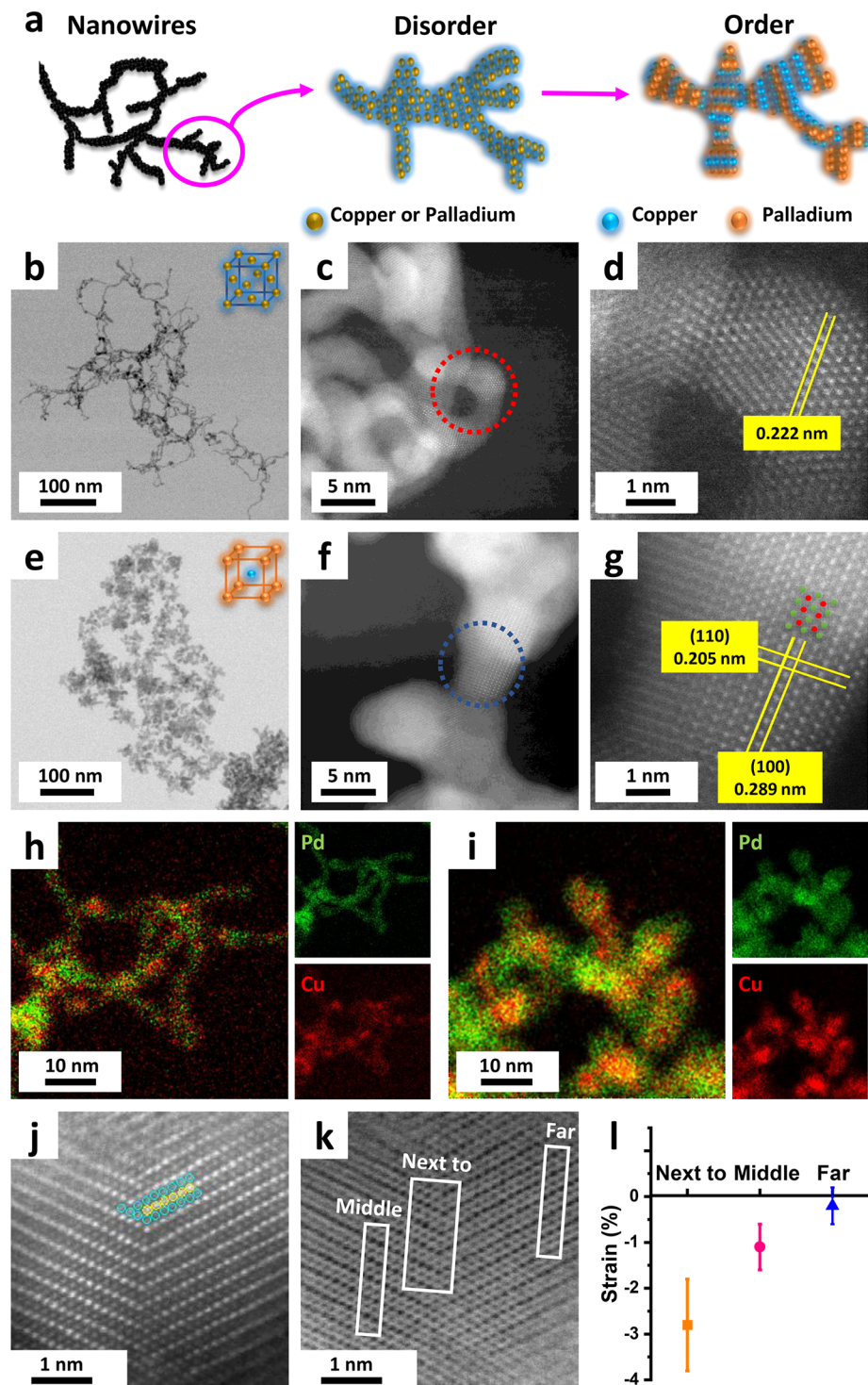


Figure 1. (a) Scheme for synthesis of the PdCu-A1 NW network and its transformation to develop PdCu-B2 NWs. (b–d) BF image. (c, d) HAADF images. (d) Zoom in corresponding to the red circle area in (c). (e–g) PdCu-B2 NWs. (e) BF image. (f, g) HAADF images, where blue circle in (f) corresponds to the image in (g). The yellow lines in (d, g) indicate the orientation of lattice plane. The noted interplanar spacing is an average of multiple lattice planes. Overlapped and individual (small panel) elemental map of PdCu-A1 (h) and PdCu-B2 (i) based on EDS spectra. Green represents Pd, and red represents Cu. (j) HAADF images of PdCu-B2 NWs showing area of twin defects at the tips of the ordered structure. Yellow circle indicates Pd, while blue circle indicates Cu. (k) BF image taken at the similar area as (j) indicating strain measurement locations. (l) Strain percentage measurement in three different locations related to the location of the twin boundary: next to, middle, and far from the boundary. Each data point corresponds to an average over six analyses.

providing a path for nontoxic and nonflammable alternatives toward greener energies.^{15,17,18}

Herein, we report the synthesis of ultrathin palladium–copper random alloy nanowires labeled as PdCu-A1 NWs.

Transformation from the A1 phase to the intermetallic B2 phase has been observed in the PdCu NWs through an electrochemical treatment at room temperature. The intermetallic B2 phase containing NWs was denoted as PdCu-B2

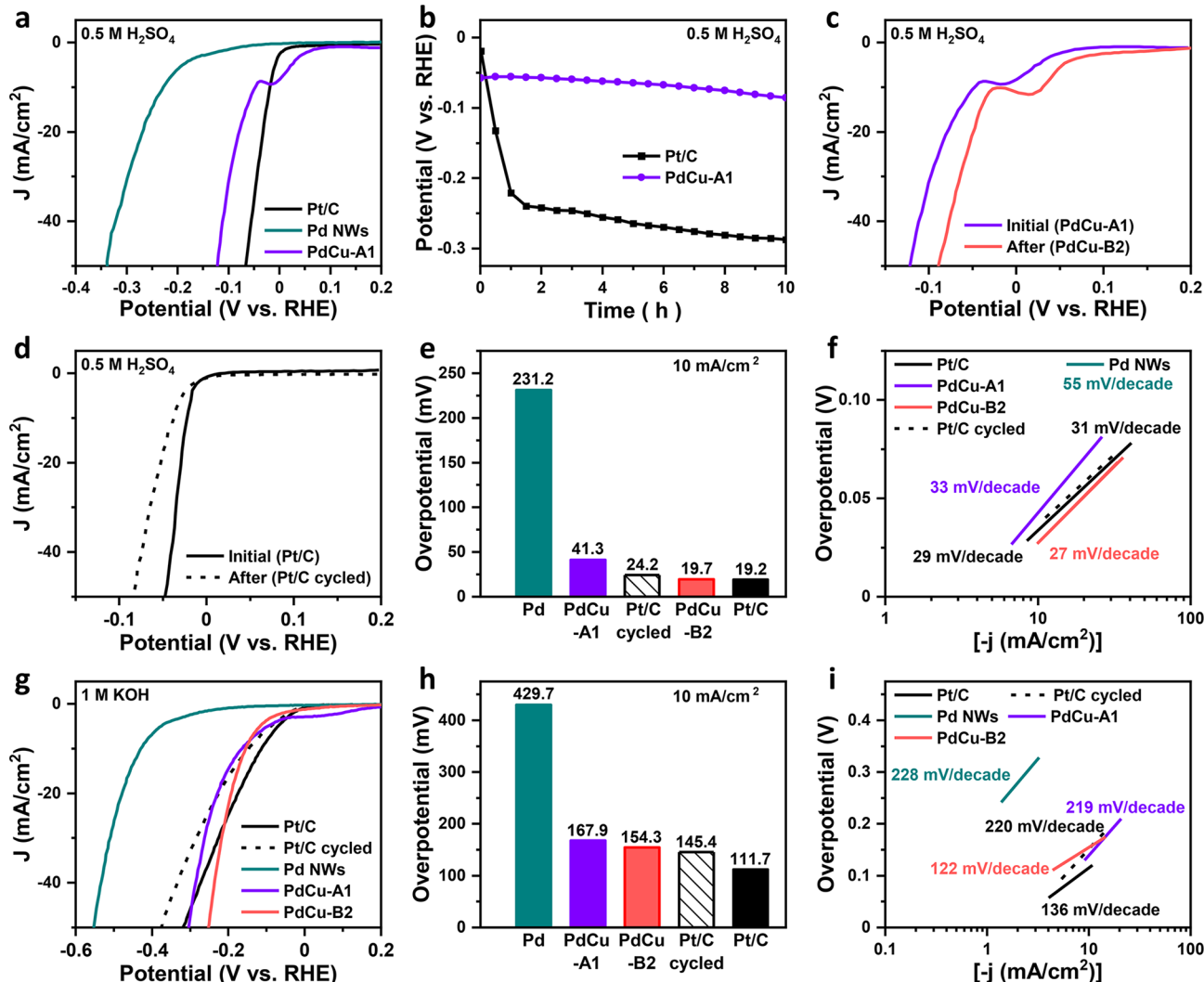


Figure 2. HER electrochemical performance of the as-synthesized PdCu-A1 NWs, PdCu-B2 NWs, Pd NWs, commercial Pt/C, and Pt/C cycled (sample tested in acidic media for 10 h) in acidic condition of 0.5 M H_2SO_4 (a–f) and basic condition of 1 M KOH (g–i). (a, c, d, g) HER polarization curves. (b) Transformation of PdCu-A1 NWs into PdCu-B2 NWs after 10 h reaction in 0.5 M H_2SO_4 and its comparison with commercial Pt/C under the same conditions transforming to Pt/C cycled (e, h) overpotential at 10 mA/cm². (f, i) corresponding Tafel plots. All the polarization curves were recorded with a scan rate of 20 mV/s and a rotation rate of 1600 rpm, and all the current densities were normalized to the geometric area of the working electrode. PdCu-A1 NWs, PdCu-B2 NWs are abbreviated as PdCu-A1 and PdCu-B2 in all figures, respectively.

NWs (Figure 1a). The synthesized PdCu-A1 NWs presented a superior ECSA and enhanced HER compared with pure palladium (Pd) NWs. Moreover, the PdCu-B2 NWs exhibit record-high HER performance in acidic media at a low overpotential of 19.7 mV at 10 mA/cm², a low Tafel slope of 27 mV/decade, and an high exchange current density of 4.7 mA/cm², superior to PdCu-A1 NWs, Pd NWs, and even commercial Pt/C. Similar advantages were observed during HER in alkaline media. In addition, with an extra-high ECSA of 116 m²/g, PdCu-B2 NWs presented the highest mass activity (MA) of 3735 mA/mg_{Pd} at the lowest onset potentials during FAOR among all the studied materials, which is almost 7 times higher than the MA of commercial Pd/C.

The PdCu-A1 NW network was obtained following reported procedures.^{37,38} In a typical synthesis, dihydrogen tetrachloropalladate (H_2PdCl_4) and copper(II) chloride (CuCl_2) were mixed in water solution containing Triton X-100 (0.2% v/v) and then reduced in the presence of NaBH_4 (Figure S1). The

products were collected by centrifuge and washed five times with ethanol/water (details noted in the Supporting Information). Transmission electron microscopy (TEM) images showed the network morphology of the product (Figure 1b). The atomic resolution high angle annular dark field-scanning transmission electron microscopy (HAADF-STEM) images in Figure 1c and d suggest that Pd and Cu form an alloy face centered cubic (fcc) structure (phase A1) as indicated by a *d*-spacing of 0.222 ± 0.001 nm corresponding to a (111) interplanar distance. Energy dispersive spectroscopy (EDS) mapping (Figures 1h and S2) showed even distribution of Pd and Cu atoms along the NW structure. The alloy PdCu-A1 NWs showed an average body diameter of around 3.5 ± 0.8 nm and a larger average diameter of 5.0 ± 0.9 nm at the tips/junctions (Figure S3). X-ray powder diffraction (XRD) studies confirmed the alloy formation with a face center cubic (fcc) packing and lattice parameter of about 0.3850 nm (Figure S4). We hence named the as-synthesized NWs as PdCu-A1 NWs.

Based on the *d*-spacing of the bright field (BF) STEM images and XRD spectrum, the approximated overall Pd/Cu atomic ratio using Vegard's law was $\text{Pd}_{85}\text{Cu}_{15}$, which is close to the composition ratio extracted from energy dispersive spectroscopy (EDS) (Pd 84%, Cu 16%) and inductively coupled plasma atomic emission spectroscopy (ICP-AES) (Pd 83.8% and Cu 16.2%). Furthermore, X-ray photoelectron spectroscopy (XPS) revealed a ratio of Pd 91% and Cu 9%, suggesting a Pd-rich surface (Figure S5).

These PdCu-A1 NWs were then treated in an electrochemical process at room temperature in acidic media that allowed Pd and Cu atoms to rearrange toward a more ordered structure (B2-intermetallic rich phase). The sample was loaded on a glassy carbon electrode and maintained in N_2 -saturated 0.5 M H_2SO_4 at a constant current density of 10 mA/cm² and at a constant rotation rate of 1600 rpm for 10 h. HER tests on the produced materials showed superior performance with lower overpotentials compared to the initial PdCu-A1 sample and even slightly better than commercial Pt/C, as shown in detail in Figure 2a–f.

We hence performed additional structural and compositional characterizations to identify these electrochemically treated PdCu-A1 samples. The TEM image in Figure 1e shows the preserved interconnected structure. However, the overall longitude and diameter of the NWs changed. Size distribution analysis based on BF STEM images showed that the treated NWs became noticeably shorter and were around 2 nm wider compared to their initial PdCu-A1 structure (Figures 1 and S3). Interestingly, HAADF STEM images (Figure 1f, g) showed the appearance of an ordered PdCu-B2 phase mostly evident at the tips and junctions of the NWs with typical *d*-spacings of around 0.205 ± 0.012 nm corresponding to the B2 (110) plane and 0.289 ± 0.002 nm corresponding to the B2 (100) plane. Moreover, atomic rows with different contrast were clearly observable in the BF and HAADF images (Figures 1g and S6), which confirmed the ordering of the Pd and Cu atoms after the electrochemical treatment process.^{33,39,40} EDS mapping (Figure 1i) of the processed sample also showed clearly a good distribution of Pd and Cu atoms, especially at the tips and junctions of the NW structure. More detailed studies of the processed sample (Figure S7) proved that the structure exhibited an ordered phase which was more evident at the tips and junctions of the NWs, with some remaining A1-phase in their body. The EDS analysis of the ordered areas suggests a ratio composition of $\text{Pd}_{56}\text{Cu}_{44}$ (Figure S8) which agrees with composition of the PdCu B2-phase as suggested by the BF and HAADF images. On the basis of these observations, we designated the new structure as PdCu-B2 NWs to indicate the formation of the B2 phase in the NW structure (Figures 1e–g and S6–S8). The BF and HAADF studies on PdCu-B2 NWs also indicated the presence of lattice strain around twin boundaries. The twin defects observed in Figure 1j were taken at the tips of the PdCu-B2 NWs, which were also observed at the junctions of the material as shown in Figure S8 (c and d, respectively). Importantly, compressive strain was observed around these twin boundaries (Figure 1k, l), which has been reported to a play role in modifying the catalytic properties of the PdCu-B2.^{41–43}

The overall composition analysis of the newly transformed PdCu-B2 NWs suggested an eventual loss of Pd compared to Cu, during the electrochemical process. This could be partially attributed to Pd-rich surface of PdCu-A1 (Figure S5), although detachment of PdCu-A1 fragments can also occur during the

treatment process. In addition, the absence of the Cu oxidation peaks⁴⁴ indicated that Cu atoms were embedded from the beginning and hence better protected against dissolution. Further evidence of absence of Cu on the surface was provided by the absence of the typical Cu oxidation peaks during the cyclic voltammetry (CV) measurement (Figure S12).⁴⁴

We investigated the electrocatalytic HER activities of PdCu-A1 and PdCu-B2 NWs, and compared their performances against our synthesized Pd NWs and commercial Pt/C in a standard three electrode electrochemical cell in acid (0.5 M H_2SO_4) and alkaline media (1 M KOH) (see the Supporting Information for details). Representative linear sweep voltammetry (LSV) of geometric current density (mA/cm²) vs RHE results for these catalysts are shown in Figure 2. HER performance in acid media is reported in Figure 2a–f, whereas alkaline media results are shown in Figure 2g–i. All potentials reported were against reversible hydrogen electrode (RHE) and *iR* compensations were applied in all data unless specifically noted.

We first compared the HER activities of PdCu-A1 NWs, Pd NWs, and commercial Pt/C under acidic conditions (Figure 2a). It was observed that, to obtain a current density of 10 mA/cm², an overpotential of 41.3 mV was required for PdCu-A1, which was much lower than that exhibited by Pd NWs (231.2 mV) but almost twice as high as that of Pt/C (19.2 mV) (Figure 2e, Table 1). In addition, the PdCu-A1 NWs

Table 1. Comparison of HER Performance in Acidic Conditions for State of the Art Pd- and Pt-Based Catalysts^a

| sample | catalyst loading, $\mu\text{g}/\text{cm}^2$ | η at 10 mA/cm ² , mV | Tafel slope, mV/dec | source |
|-------------------|---|--------------------------------------|---------------------|-----------|
| PdCu-B2 NWs | 51 | 19.7 | 27 | this work |
| PdCu-A1 NWs | 51 | 41.3 | 33 | this work |
| Pd NWs | 51 | 231.2 | 55 | this work |
| Pt/C | 51 | 19.2 | 29 | this work |
| PdCu@PdNCs | 140 | 68 | 35 | ref 8 |
| Pd–Cu–S amorphous | ~660 | 58 | 35 | ref 47 |
| Pd-CNx np | 43 | 55 | 35 | ref 2 |

^aNote: dec is short for decade.

presented a Tafel slope of 33 mV/decade which is close to that of commercial Pt/C (29 mV/decade) (Figure 2f) and much smaller than that of the Pd NWs (55 mV/decade) (Figure S9), following a Volmer–Tafel mechanism.^{2,45} Chronopotentiometry tests (stability tests) in acidic media (0.5 M H_2SO_4) at 10 mA/cm² showed that PdCu-A1 NWs outperformed commercial Pt/C in terms of stability and induced the electrochemical transformation of PdCu-A1 NWs to PdCu-B2 NWs (Figure 2b). After cycling tests in acidic media, HER catalytic activities were investigated on the final samples, PdCu-B2 NWs and Pt/C cycled. Surprisingly, HER catalytic activity of PdCu-B2-NWs improved significantly compared to its initial counterpart PdCuA1 NWs (Figure 2c), whereas commercial Pt/C cycled performed worse than its initial counterpart commercial Pt/C (Figure 2d).

Impressively, from all the studied catalysts, PdCu-B2 NWs showed outstanding in performance for HER in acidic media with an overpotential of 19.7 mV, comparable to that of

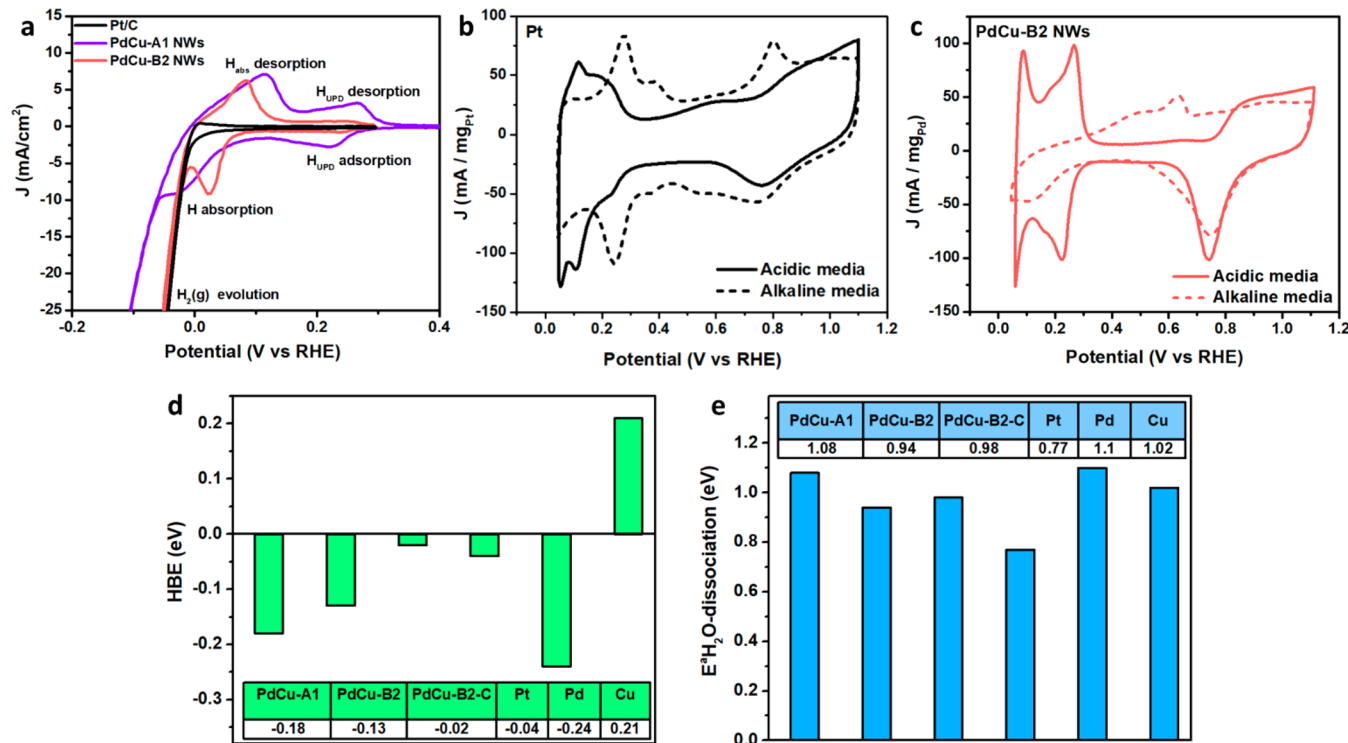


Figure 3. (a) CV profile acquired in 0.5 M H_2SO_4 solution at a scan rate of 20 mV/s in the range of −0.2 to 0.4 V vs RHE for Pt/C, PdCu-A1, and PdCu-B2 NWs. (b, c) CV curves acquired in acidic and alkaline media at a scan rate of 100 mV/s in the range of 0.05–1.1 V vs RHE of (b) Pt/C and (c) PdCu-B2 NWs. (d) DFT calculated hydrogen binding energies (HBEs). (e) DFT calculated reaction barrier for water dissociation ($E_a(\text{H}_2\text{O-dissociation})$).

commercial Pt/C, while it exhibited a Tafel slope of 27 mV/decade, similar to and slightly smaller than commercial Pt/C. The Tafel slope decreases in the order of Pd NWs > PdCu-A1 > Pt/C cycled > Pt/C > PdCu-B2 (Figure 2f; Tables 1 and S2), indicating the fastest HER reaction kinetics on the PdCu-B2 surface even when compared to commercial Pt/C. Meanwhile, PdCu-B2 also exhibited a much higher exchange current density of 4.7 mA/cm^2 when compared to commercial Pt/C, PdCu-A1 (both ca. 3.2 mA/cm^2) and Pd NWs (0.02 mA/cm^2). These observations are in agreement with previous literature where a smaller Tafel slope usually leads to higher exchange current densities, and a smaller overpotential signifies the HER rate can gain a faster increase at a competitive potential for practical applications.⁴⁶ Indeed, to obtain a current density of 50 mA/cm^2 , an overpotential of 90 mV was sufficient with PdCu-B2, which was lower than the comparison samples (Table S2). Thus, these results suggest that PdCu-B2 display the best HER kinetics among all electrocatalysts investigated in acid media here.

Additionally, PdCu-A1 and PdCu-B2 curves in Figure 2c suggest typical presence of hydrogen absorption peaks (H_{abs}) in the range of 0.0–0.05 V. Thus, we ran a full CV profile for PdCu-A1 as an example (Figure S10) and identified asymmetrical anodic and cathodic peaks at around 0.21 and 0.26 V corresponding to underpotential hydrogen adsorption (UPD- H_{ads}) and desorption (UPD- H_{des}) peaks, respectively. In addition, asymmetrical peaks at a range around −0.03 and 0.11 V were also observed, corresponding to overpotential hydrogen absorption (OPD- H_{abs}) and desorption (OPD- H_{des}), respectively.^{2,21} Lastly, PdCu-B2 showed an impressive ECSA (Figures S11 and S12; Table S1), especially a high ECSA_{CO}

around 116 m^2/g from CO stripping measurements, which will contribute to its eventual high mass activity as electrocatalysts.

The performance of the PdCu-A1 and PdCu-B2 catalysts were also investigated in alkaline solution (1 M KOH) and compared to Pd NWs and commercial Pt/C (Figure 2g–i). Previous reports have established that, in neutral and alkaline solutions, the HER mechanism may be different from that in acidic solution, where not only HBE plays a role but also the HO–H bond in H_2O and its dissociation play a crucial role in the whole HER process.^{5,25,45} LSV curves in Figure 2g and overpotential bars in Figure 2h show that, to obtain a current density of 10 mA/cm^2 , PdCu-B2 NWs needed an overpotential of 154.3 mV which is lower than their PdCu-A1 counterpart and comparable with Pt/C. Surprisingly, in order to obtain a higher current density of 50 mA/cm^2 , PdCu-B2 NWs required the lowest overpotential than the other catalysts (Figure S13; Table S3). In fact, PdCu-B2 NWs required an overpotential of only 247.9 mV versus 303.7, 316.4, and 547.1 mV of PdCu-A1 NWs, Pt/C, and Pd NWs, respectively. Tafel slopes corroborated the result for PdCu-B2 NWs in alkaline media showing a smaller slope of around 122 mV/decade than Pt/C which exhibited a slope of 136 mV/decade. The rest of the catalysts exhibited much higher values in Tafel slopes (Figure 2i; Table S3). Once again, these results suggested better kinetics for PdCu-B2 NWs in alkaline media than PdCu-A1 and commercial Pt/C. Furthermore, chronopotentiometry tests were performed in alkaline media at 10 mA/cm^2 for as synthesized PdCu-A1 NWs catalysts and compared with commercial Pt/C (Figure S14). PdCu-A1 in alkaline conditions performed similarly in acidic media, exhibiting higher stability than commercial Pt/C.

In order to elucidate the mechanism of the exceptional HER enhancement observed in PdCu-B2, we performed further electrochemical analyses and DFT calculations. HBE has been suggested to directly correlate to the UPD-H_{des} peak potential, and plays a critical role during HER performance.^{45,48} We performed CV studies in both acidic and alkaline solutions and observed differences in the UPD-H_{des} peaks (Figure 3a–c). In 0.5 M H₂SO₄ solution at a scan rate of 20 mV/s in the range of −0.2 to 0.4 V, it was observed that UPD-H_{ads} and UPD-H_{des} were minimal or almost null in PdCu-B2 NWs and commercial Pt/C samples compared to PdCu-A1 NWs, where UPD-H_{ads} and UPD-H_{des} peaks were clearly observed at 0.22 and 0.26 V (Figure 3a). These results indicate that, similar to the case of Pt/C, PdCu-B2 NWs bind hydrogen at a close-to “optimal” binding strength for HER, whereas PdCu-A1 NWs may bind hydrogen too strong which leads to decreased HER activity, in agreement with previous reports.^{45,49} Moreover, PdCu-B2 (Figure 3a, red) exhibited strong OPD-H_{abs} at 0.02 V and the corresponding OPD-H_{des} peak at 0.08 V, which indicates that OPD-H_{abs} on PdCu-B2 initiates at potentials very close to the reversible H⁺/H₂ potential.² These observations allowed us to hypothesize that the optimized HBE on PdCu-B2 NWs in acid media may account for their better HER performance than Pt/C.

In addition, we compared CV curves acquired in acidic (0.5 M H₂SO₄) and alkaline media (1 M KOH) in the range of 0.05–1.1 V for Pt/C and PdCu-B2 NWs (Figure 3b, c). It is evident that the UPD-H peaks shifted to a more positive potential in both catalysts, suggesting a slower HER kinetics in alkaline media compared to acidic media. This agrees with literature suggested trend in decreasing HER activity in alkaline conditions when compared to acid conditions for nanocatalyst based on Pd, Pt, Ir, and Rh elements.^{2,25,45,50,51}

To obtain further understanding of the high HER activity on PdCu-B2 in both acid and alkaline media, we performed DFT studies (PBE-D3-flavor). The calculated HBEs and Ea_{H₂O} dissociation results for different catalysts are shown in Figure 3d and e. Calculations for oxygen reduction reaction (ORR) on the B2 phase were reported previously.⁵² We calculated the HBEs of the experimentally investigated systems: PdCu-A1 (Pd₈₄Cu₁₆), PdCu-B2, compressed PdCu-B2, Pt, Pd, and Cu (more details about the models are provided in the Supporting Information). As shown in Figure 3d, the calculated HBEs are −0.18 eV for PdCu-A1, −0.13 eV for PdCu-B2, −0.02 eV for compressed PdCu-B2, −0.04 eV for Pt, −0.24 eV for Pd, and 0.21 eV for Cu. Thus, the HBE of compressed PdCu-B2 is closest to zero, indicating that compressed PdCu-B2 provides the best performance at acidic conditions, which is consistent with the experiment.

We also calculated the reaction barrier for water dissociation ($E_a(H_2O\text{-dissociation})$) of the experimentally investigated systems (Figure 3e): PdCu-A1, PdCu-B2, compressed PdCu-B2 (PdCu-B2-C), Pt, Pd, and Cu. The calculated $E_a(H_2O\text{-dissociation})$ values are 1.08 eV for PdCu-A1, 0.94 eV for PdCu-B2, 0.98 eV for PdCu-B2-C, 0.77 eV for Pt, 1.10 eV for Pd, and 1.02 eV for Cu. Thus, the $E_a(H_2O\text{-dissociation})$ value of Pt is the lowest and that of PdCu-B2 is the second-lowest, indicating that Pt represents the best performance and PdCu-B2 represents the second-best performance at alkaline conditions. This is again consistent with experimental observations. Overall, the DFT calculations predict that the PdCu-B2 phase presence is responsible for the improved HER performance. Specifically, the exceptional HER performance at

acidic conditions might be attributed to the decreased HBE on the compressed PdCu-B2 phase even when compared to Pt/C, and the improved HER performance at alkaline conditions compared to PdCu-A1 might be attributed to the reduced water dissociation barriers.

Pd-based catalysts are known as excellent catalysts for electron-oxidation reaction of small molecules like FAOR, the anodic reaction in DFACFCs. In this reaction, formic acid is first adsorbed on the Pd surface to promote its dissociation, followed by a two-electron oxidation process to convert to CO₂ in a direct oxidation pathway, eliminating undesired products such as CO commonly observed on Pt-based catalysts.^{14,36,53,54} Incorporating a transition metal into the Pd catalyst promotes HO formation and thus the oxidization of CO which also increases the CO tolerance.⁵³ Hence, it suggests excellent FAOR performance on PdCu-B2 NWs. CV curves are presented in Figure 4a where Cu oxidation peaks were not

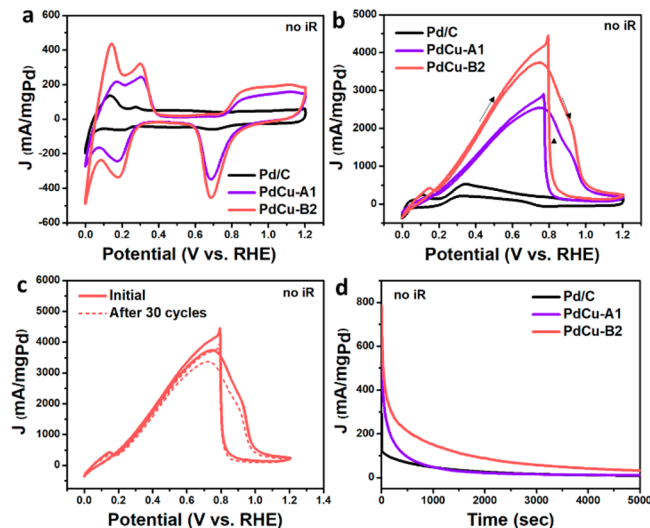


Figure 4. (a) Cyclic voltammetry (CV) curves and (b) FAOR CVs of the as-synthesized NWs PdCu-A1 NWs, PdCu-B2 NWs, and commercial Pd/C. (c) FAOR CV of initial PdCu-B2 NWs and after 30 cycles. (d) Chronoamperometry (CA) curves of the as-synthesized NWs PdCu-A1 NWs, PdCu-B2 NWs, and commercial Pd/C. CVs were obtained in N₂ saturated 0.5 M H₂SO₄ at a scan rate of 100 mV/s, and the FAOR CVs were in N₂ saturated 0.5 M H₂SO₄ + 0.5 M HCOOH with a scan rate of 50 mV/s. CA curves were recorded at 0.4 V for 5000 s in a 0.5 M H₂SO₄ + 0.5 M HCOOH solution. All the tests were conducted at room temperature.

observed in a range of 0.3–0.7 V vs RHE,¹⁰ suggesting that the NWs surface is well conditioned.⁵³ Figure 4b shows that, during the positive scan, a current was generated, indicating the oxidation of formic acid where the maximum current peak is characteristic for each catalyst tested. As it was observed, PdCu-B2 NWs exhibit the highest MA with a value of 3735 mA/mg_{Pd} which was much higher than that of PdCu-A1 (2540 mA/mg_{Pd}) and 7 times higher than that of commercial Pd/C (527 mA/mg_{Pd}). After 30 cycles of forward/backward scans, PdCu-B2 NWs still retained a mass activity of 3361 mA/mg_{Pd}, which is only 10% less than the initial mass current density (Figures 4c and S16). The MA of PdCu-B2 NWs is also superior to previously reported values (Table S4).¹⁵

FAOR curves of PdCu-A1 NWs (purple line in Figure 4b) evidenced that the main mechanism controlling the reaction is

through directly dehydrogenation of formic acid toward CO₂ production. Nonetheless, a small shoulder during the positive scan at around 0.9 V vs RHE indicates that FAOR still undergoes an intermediate dehydration pathway (CO + H₂O). This shoulder, corresponding to CO, is slightly reduced during FAOR on PdCu-B2 (red line in Figure 4b), suggesting a better dehydrogenation process.^{36,53} Meanwhile, the onset potential was much lower in PdCu-B2 (0.168 V) compared to the PdCu-A1 alloy (0.178 V) and commercial Pd/C (0.188 V). Moreover, the sharp peaks observed at around 0.8 V in the negative scan for both PdCu-A1 and PdCu-B2 NWs indicated that the catalyst surface was regenerated via surface reduction, as observed by the sudden jump in the current. These observations suggested that Pd in the PdCu-B2 and PdCu-A1 NWs was reduced more efficiently than the Pd in commercial Pd/C, in agreement with previous literature.^{14,15} Thus, the higher oxidation peak value for mass activity and the lower onset potential demonstrated that the electrooxidation activity for FAOR is favored in PdCu-B2 NWs.^{15,55–58} Finally, stability tests were performed (Figure 4d). In the first 250 s, commercial Pd/C decayed very fast. After 1000 s, PdCu-A1 and commercial Pd/C showed equivalent current densities, suggesting similar stability in the later stage, while PdCu-B2 NWs exhibited better stability and displayed higher mass current density than PdCu-A1 and commercial Pd/C throughout the test. After the stability tests, no significant morphology changes of PdCu-B2 NWs were observed (Figure S15).

In summary, we have demonstrated the transformation of alloy A1 phase into intermetallic B2 phase through the electrochemical treatment of the PdCu NW networks. Impressively, the NWs containing the PdCu-B2 phase demonstrated enhanced electrocatalytic activity toward HER in acid and alkaline conditions, showing even higher HER activity and electrochemical surface area than those of commercial Pt/C in acids. DFT calculations demonstrated that the improved HER performance at acidic conditions can be attributed to the decreased HBE due to the presence of a compressed PdCu-B2 phase, while the improved HER performance compared to PdCu-A1 at alkaline conditions can be attributed to the reduced water dissociation energy barrier. In addition, both PdCu-A1 and PdCu-B2 demonstrated superior FAOR activities, with PdCu-B2 showing the highest MA compared to reported values. This work provides an alternative approach to design and develop electrocatalysts with outstanding performance for diverse reactions that can enable practical applications.

ASSOCIATED CONTENT

Supporting Information

The Supporting Information is available free of charge at <https://pubs.acs.org/doi/10.1021/acsenergylett.0c01959>.

Materials and methods, as well as supplementary data (PDF)

AUTHOR INFORMATION

Corresponding Authors

Zipeng Zhao — Department of Materials Science and Engineering, University of California, Los Angeles, California 90095, United States; orcid.org/0000-0003-1135-6742; Email: zipeng.zhao@ucla.edu

Yu Huang — Department of Materials Science and Engineering and California NanoSystems Institute, University of California, Los Angeles, California 90095, United States; orcid.org/0000-0003-1793-0741; Email: yhuang@seas.ucla.edu

Authors

Michelle M. Flores Espinosa — Department of Materials Science and Engineering, University of California, Los Angeles, California 90095, United States; orcid.org/0000-0002-5697-1290

Tao Cheng — Materials and Process Simulation Center, California Institute of Technology, Pasadena, California 91125, United States; Institute of Functional Nano & Soft Materials (FUNSOM), Jiangsu Key Laboratory for Carbon-Based Functional Materials & Devices, Joint International Research Laboratory of Carbon-Based Functional Materials and Devices, Soochow University, Suzhou 215123, Jiangsu, China; orcid.org/0000-0003-4830-177X

Mingjie Xu — Irvine Materials Research Institute and Department of Chemical Engineering and Materials Science, University of California, Irvine, California 92697, United States; Department Fok Ying Tung Research Institute, Hong Kong University of Science and Technology, Guangzhou 511458, P. R. China

Luca Abatemarco — Department of Chemistry and Biochemistry, University of California, Los Angeles, California 90095, United States

Chungseok Choi — Department of Materials Science and Engineering, University of California, Los Angeles, California 90095, United States; orcid.org/0000-0001-9169-1393

Xiaoqing Pan — Irvine Materials Research Institute, Department of Chemical Engineering and Materials Science, and Department of Physics and Astronomy, University of California, Irvine, California 92697, United States; orcid.org/0000-0002-0965-8568

William A. Goddard, III — Materials and Process Simulation Center, California Institute of Technology, Pasadena, California 91125, United States; orcid.org/0000-0003-0097-5716

Complete contact information is available at:
<https://pubs.acs.org/10.1021/acsenergylett.0c01959>

Notes

The authors declare no competing financial interest.

ACKNOWLEDGMENTS

Y.H., W.A.G., Z.Z., and M.F.E. acknowledge the support from Office of Naval Research (N000141812155). T.C. was supported by the Collaborative Innovation Center of Suzhou Nano Science & Technology, the Priority Academic Program Development of Jiangsu Higher Education Institutions (PAPD) and the 111 Project. W.A.G. was supported by the Joint Center for Artificial Photosynthesis, a DOE Energy Innovation Hub, supported through the Office of Science of the U.S. Department of Energy under Award No. DE-SC0004993. This work used the Extreme Science and Engineering Discovery Environment (XSEDE) which is supported by National Science Foundation Grant No. ACI-1548562. The work at UC Irvine was supported by the National Science Foundation with Grants CBET 1159240, DMR1420620, and DMR-1506535. TEM work on JEM Grand ARM was conducted using the facilities in the Irvine Materials Research Institute (IMRI) at the University of California Irvine.

■ REFERENCES

- (1) Sharma, S.; Ghoshal, S. K. Hydrogen the Future Transportation Fuel: From Production to Applications. *Renewable Sustainable Energy Rev.* **2015**, *43*, 1151–1158.
- (2) Bhowmik, T.; Kundu, M. K.; Barman, S. Palladium Nanoparticle–Graphitic Carbon Nitride Porous Synergistic Catalyst for Hydrogen Evolution/Oxidation Reactions over a Broad Range of PH and Correlation of Its Catalytic Activity with Measured Hydrogen Binding Energy. *ACS Catal.* **2016**, *6*, 1929–1941.
- (3) Zhang, H.; An, P.; Zhou, W.; Guan, B. Y.; Zhang, P.; Dong, J.; Lou, X. W. D. Dynamic Tractation of Lattice-Confining Platinum Atoms into Mesoporous Carbon Matrix for Hydrogen Evolution Reaction. *Sci. Adv.* **2018**, *4*, eaao6657.
- (4) Zheng, Y.; Jiao, Y.; Zhu, Y.; Li, L. H.; Han, Y.; Chen, Y.; Jaroniec, M.; Qiao, S. High Electrocatalytic Hydrogen Evolution Activity of an Anomalous Ruthenium Catalyst. *J. Am. Chem. Soc.* **2016**, *138*, 16174–16181.
- (5) Mahmood, J.; Li, F.; Jung, S.; Okyay, M. S.; Ahmad, I.; Kim, S.; Park, N.; Jeong, H. Y.; Baek, J. An Efficient and PH-Universal Ruthenium-Based Catalyst for the Hydrogen Evolution Reaction. *Nat. Nanotechnol.* **2017**, *12*, 441–446.
- (6) Cao, L.; Luo, Q.; Liu, W.; Lin, Y.; Liu, X.; Cao, Y.; Zhang, W.; Wu, Y.; Yang, J.; Yao, T.; Wei, S. Identification of Single-Atom Active Sites in Carbon-Based Cobalt Catalysts during Electrocatalytic Hydrogen Evolution. *Nat. Catal.* **2019**, *2*, 134–141.
- (7) Zhao, Z.; Liu, H.; Gao, W.; Xue, W.; Liu, Z.; Huang, J.; Pan, X.; Huang, Y. Surface-Engineered PtNi-O Nanostructure with Record-High Performance for Electrocatalytic Hydrogen Evolution Reaction. *J. Am. Chem. Soc.* **2018**, *140*, 9046–9050.
- (8) Li, J.; Li, F.; Guo, S.; Zhang, J.; Ma, J. PdCu @ Pd Nanocube with Pt-like Activity for Hydrogen Evolution Reaction. *ACS Appl. Mater. Interfaces* **2017**, *9*, 8151–8160.
- (9) Li, M.; Duanmu, K.; Wan, C.; Cheng, T.; Zhang, L.; Dai, S.; Chen, W.; Zhao, Z.; Li, P.; Fei, H.; Zhu, Y.; Yu, R.; Luo, J.; Zang, K.; Lin, Z.; Ding, M.; Huang, J.; Sun, H.; Guo, J.; Pan, X.; Goddard, W. A., III; Sautet, P.; Huang, Y.; Duan, X. Single-Atom Tailoring of Platinum Nanocatalysts for High-Performance Multifunctional Electrocatalysis. *Nat. Catal.* **2019**, *2*, 495–503.
- (10) Wu, D.; Xu, H.; Cao, D.; Fisher, A.; Gao, Y.; Cheng, D. PdCu Alloy Nanoparticle-Decorated Copper Nanotubes as Enhanced Electrocatalysts: DFT Prediction Validated by Experiment. *Nanotechnology* **2016**, *27*, 495403.
- (11) Zhao, X.; Dai, L.; Qin, Q.; Pei, F.; Hu, C.; Zheng, N. Self-Supported 3D PdCu Alloy Nanosheets as a Bifunctional Catalyst for Electrochemical Reforming of Ethanol. *Small* **2017**, *13*, 1602970.
- (12) Zhao, Z.; Flores Espinosa, M. M.; Zhou, J.; Xue, W.; Duan, X.; Miao, J.; Huang, Y. Synthesis of Surface Controlled Nickel/Palladium Hydride Nanodendrites with High Performance in Benzyl Alcohol Oxidation. *Nano Res.* **2019**, *12*, 1467–1472.
- (13) Wen, C.; Wei, Y.; Tang, Di.; Sa, B.; Zhang, T.; Chen, C. Improving the Electrocatalytic Properties of Pd-Based Catalyst for Direct Alcohol Fuel Cells: Effect of Solid Solution. *Sci. Rep.* **2017**, *7*, 1–11.
- (14) Mazumder, V.; Chi, M.; Mankin, M. N.; Liu, Y.; Metin, Ö.; Sun, D.; More, K. L.; Sun, S. A Facile Synthesis of MPd (M = Co, Cu) Nanoparticles and Their Catalysis for Formic Acid Oxidation. *Nano Lett.* **2012**, *12*, 1102–1106.
- (15) Li, S.; Cheng, D.; Qiu, X.; Cao, D. Synthesis of Cu@Pd Core-Shell Nanowires with Enhanced Activity and Stability for Formic Acid Oxidation. *Electrochim. Acta* **2014**, *143*, 44–48.
- (16) Li, C.; Yuan, Q.; Ni, B.; He, T.; Zhang, S.; Long, Y.; Gu, L.; Wang, X. Dendritic Defect-Rich Palladium-Copper-Cobalt Nanoalloys as Robust Multifunctional Non-Platinum Electrocatalysts for Fuel Cells. *Nat. Commun.* **2018**, *9*, 1–9.
- (17) Bin, D.; Yang, B.; Ren, F.; Zhang, K.; Yang, P.; Du, Y. Facile Synthesis of PdNi Nanowire Networks Supported on Reduced Graphene Oxide with Enhanced Catalytic Performance for Formic Acid. *J. Mater. Chem. A* **2015**, *3*, 14001–14006.
- (18) Liu, Z.; Fu, G.; Li, J.; Liu, Z.; Xu, L.; Sun, D.; Tang, Y. Facile Synthesis Based on Novel Carbon-Supported Cyanogel of Structurally Ordered Pd3Fe/C as Electrocatalyst for Formic Acid Oxidation. *Nano Res.* **2018**, *11*, 4686–4696.
- (19) Yao, R.-Q.; Zhou, Y.-T.; Shi, H.; Zhang, Q.-H.; Gu, L.; Wen, Z.; Lang, X.-Y.; Jiang, Q.; et al. Nanoporous Palladium-Silver Surface Alloys as Efficient and PH-Universal Catalysts for the Hydrogen Evolution Reaction. *ACS Energy Lett.* **2019**, *4*, 1379–1386.
- (20) Li, M.; Luo, M.; Xia, Z.; Yang, Y.; Huang, Y.; Wu, D.; Sun, Y.; Li, C.; Chao, Y.; Yang, W.; Yang, W.; Yu, Y.; Guo, S. Modulating Surface Segregation of PdCuRu Nanocrystals for Enhanced All-PH Hydrogen Evolution Electrocatalysis. *J. Mater. Chem. A* **2019**, *7*, 20151–20157.
- (21) Zalineeva, A.; Baranton, S.; Coutanceau, C.; Jerkiewicz, G. Octahedral Palladium Nanoparticles as Excellent Hosts for Electrochemically Adsorbed and Absorbed Hydrogen. *Sci. Adv.* **2017**, *3*, e1600542.
- (22) Li, M.; Li, M.; Zhao, Z.; Cheng, T.; Fortunelli, A.; Chen, C.; Yu, R.; Gu, L.; Merinov, B.; Lin, Z.; Zhu, E.; Yu, T.; Jia, Q.; Guo, J.; Zhang, L.; Goddard, W. A., III; Huang, Y.; Duan, X. Ultrafine Jagged Platinum Nanowires Enable Ultrahigh Mass Activity for the Oxygen Reduction Reaction. *Science* **2016**, *354*, 1414–1419.
- (23) Fu, X.; Zhao, Z.; Wan, C.; Wang, Y.; Fan, Z.; Song, F.; Cao, B.; Li, M.; Xue, W.; Huang, Y.; Duan, X. Ultrathin Wavy Rh Nanowires as Highly Effective Electrocatalysts for Methanol Oxidation Reaction with Ultrahigh ECSA. *Nano Res.* **2019**, *12*, 211–215.
- (24) Huang, H.; Ruditskiy, A.; Choi, S. Il; Zhang, L.; Liu, J.; Ye, Z.; Xia, Y. One-Pot Synthesis of Penta-Twinned Palladium Nanowires and Their Enhanced Electrocatalytic Properties. *ACS Appl. Mater. Interfaces* **2017**, *9*, 31203–31212.
- (25) Qiu, Y.; Xin, L.; Li, Y.; McCrum, I. T.; Guo, F.; Ma, T.; Ren, Y.; Liu, Q.; Zhou, L.; Gu, S.; Janik, M. J.; Li, W. BCC-Phased PdCu Alloy as a Highly Active Electrocatalyst for Hydrogen Oxidation in Alkaline Electrolytes. *J. Am. Chem. Soc.* **2018**, *140*, 16580–16588.
- (26) Wang, Y.; Hall, A. S. Pulsed Electrodeposition of Metastable Pd31Bi12 Nanoparticles for Oxygen Reduction Electrocatalysis. *ACS Energy Lett.* **2020**, *5*, 17–22.
- (27) Qin, Y.; Luo, M.; Sun, Y.; Li, C.; Huang, B.; Yang, Y.; Li, Y.; Wang, L.; Guo, S. Intermetallic Hcp -PtBi/Fcc -Pt Core/Shell Nanoplates Enable Efficient Bifunctional Oxygen Reduction and Methanol Oxidation Electrocatalysis. *ACS Catal.* **2018**, *8*, 5581–5590.
- (28) Kim, H. Y.; Kim, J. M.; Ha, Y.; Woo, J.; Byun, A.; Shin, T. J.; Park, K. H.; Jeong, H. Y.; Kim, H.; Kim, J. Y.; Joo, S. H. Activity Origin and Multifunctionality of Pt-Based Intermetallic Nanostructures for Efficient Electrocatalysis. *ACS Catal.* **2019**, *9*, 11242–11254.
- (29) Jiang, K.; Wang, P.; Guo, S.; Zhang, X.; Shen, X.; Lu, G.; Su, D.; Huang, X. Ordered PdCu-Based Nanoparticles as Bifunctional Oxygen-Reduction and Ethanol-Oxidation Electrocatalysts. *Angew. Chem.* **2016**, *128*, 9176–9181.
- (30) Kim, H. Y.; Joo, S. H. Recent Advances in Nanostructured Intermetallic Electrocatalysts for Renewable Energy Conversion. *J. Mater. Chem. A* **2020**, *8*, 8195–8217.
- (31) Wang, C.; Chen, D. P.; Sang, X.; Unocic, R. R.; Skrabalak, S. E. Size-Dependent Disorder-Order Transformation in the Synthesis of Monodisperse Intermetallic PdCu Nanocatalysts. *ACS Nano* **2016**, *10*, 6345–6353.
- (32) Shi, Q.; Zhu, C.; Bi, C.; Xia, H.; Engelhard, M. H.; Du, D.; Lin, Y. Intermetallic Pd3Pb Nanowire Networks Boost Ethanol Oxidation and Oxygen Reduction Reactions with Significantly Improved Methanol Tolerance. *J. Mater. Chem. A* **2017**, *5*, 23952–23959.
- (33) Bu, L.; Zhang, X.; Shen, X.; Su, D.; Lu, G.; Zhu, X.; Yao, J.; Guo, J.; Guo, S.; Huang, X. Surface Engineering of Hierarchical Platinum-Cobalt Nanowires for Efficient Electrocatalysis. *Nat. Commun.* **2016**, *7*, 11850.
- (34) Li, M.; Xia, Z.; Huang, Y.; Tao, L.; Chao, Y.; Yin, K.; Yang, W.; Yang, W.; Yu, Y.; Guo, S. Rh-Doped PdCu Ordered Intermetallics for Enhanced Oxygen Reduction Electrocatalysis with Superior Methanol Tolerance. *Acta Phys.-Chim. Sin.* **2020**, *36*, 1912040–1912049.

- (35) Zhang, J.; Chen, M.; Li, H.; Li, Y.; Ye, J.; Cao, Z.; Fang, M.; Kuang, Q.; Zheng, J.; Xie, Z. Stable Palladium Hydride as a Superior Anode Electrocatalyst for Direct Formic Acid Fuel Cells. *Nano Energy* **2018**, *44*, 127–134.
- (36) Xi, Z.; Erdosy, D. P.; Mendoza-Garcia, A.; Duchesne, P. N.; Li, J.; Muzzio, M.; Li, Q.; Zhang, P.; Sun, S. Pd Nanoparticles Coupled to WO_{2.72} Nanorods for Enhanced Electrochemical Oxidation of Formic Acid. *Nano Lett.* **2017**, *17*, 2727–2731.
- (37) Lv, J.; Wang, Z.; Feng, J.; Qiu, R.; Wang, A.; Xu, X. Facile Synthesis of Highly Active Pd-Cu Nanowires Catalyst through a Simple Wet-Chemical Strategy for Ligand-Free Suzuki Cross Coupling Reaction. *Appl. Catal., A* **2016**, *522*, 188–193.
- (38) Yuan, T.; Wang, A.; Fang, K.; Wang, Z.; Feng, J. Hydrogen Evolution-Assisted One-Pot Aqueous Synthesis of Hierarchical Trimetallic PdNiRu Nanochains for Hydrazine Oxidation Reaction. *J. Energy Chem.* **2017**, *26*, 1231–1237.
- (39) Rong, H.; Mao, J.; Xin, P.; He, D.; Chen, Y.; Wang, D.; Niu, Z.; Wu, Y.; Li, Y. Kinetically Controlling Surface Structure to Construct Defect-Rich Intermetallic Nanocrystals: Effective and Stable Catalysts. *Adv. Mater.* **2016**, *28*, 2540–2546.
- (40) Li, J.; Xi, Z.; Pan, Y.; Spendelow, J. S.; Duchesne, P. N.; Su, D.; Li, Q.; Yu, C.; Yin, Z.; Shen, B.; Kim, Y. S.; Zhang, P.; Sun, S. Fe Stabilization by Intermetallic L10 - FePt and Pt Catalysis Enhancement in L10 - FePt/Pt Nanoparticles for Efficient Oxygen Reduction Reaction in Fuel Cells. *J. Am. Chem. Soc.* **2018**, *140*, 2926–2932.
- (41) Yao, Y.; Hu, S.; Chen, W.; Huang, Z.-Q.; Wei, W.; Yao, T.; Liu, R.; Zang, K.; Wang, X.; Wu, G.; Yuan, W.; Yuan, T.; Zhu, B.; Liu, W.; Li, Z.; He, D.; Xue, Z.; Wang, Y.; Zheng, X.; Dong, J.; Chang, C.-R.; Chen, Y.; Hong, X.; Luo, J.; Wei, S.; Li, W.-X.; Strasser, P.; Wu, Y.; Li, Y. Engineering the Electronic Structure of Single Atom Ru Sites via Compressive Strain Boosts Acidic Water Oxidation Electrocatalysis. *Nat. Catal.* **2019**, *2*, 304–313.
- (42) Luo, M.; Guo, S. Strain-Controlled Electrocatalysis on Multimetallic Nanomaterials. *Nat. Rev. Mater.* **2017**, *2*, 17059.
- (43) Wang, L.; Zeng, Z.; Gao, W.; Maxson, T.; Raciti, D.; Giroux, M.; Pan, X.; Wang, C.; Greeley, J. Tunable Intrinsic Strain in Two-Dimensional Transition Metal Electrocatalysts. *Science* **2019**, *363*, 870–874.
- (44) Jana, R.; Bhim, A.; Bothra, P.; Pati, S. K.; Peter, S. C. Electrochemical Dealloying of PdCu₃ Nanoparticles to Achieve Pt-like Activity for the Hydrogen Evolution Reaction. *ChemSusChem* **2016**, *9*, 2922–2927.
- (45) Sheng, W.; Zhuang, Z.; Gao, M.; Zheng, J.; Chen, J. G.; Yan, Y. Correlating Hydrogen Oxidation and Evolution Activity on Platinum at Different PH with Measured Hydrogen Binding Energy. *Nat. Commun.* **2015**, *6*, 5848.
- (46) Chao, T.; Luo, X.; Chen, W.; Jiang, B.; Ge, J.; Lin, Y.; Wu, G.; Wang, X.; Hu, Y.; Zhuang, Z.; Wu, Y.; Hong, X.; Li, Y. Hydrogen Evolution Reaction Atomically Dispersed Copper – Platinum Dual Sites Alloyed with Palladium Nanorings Catalyze the Hydrogen Evolution Reaction Angewandte. *Angew. Chem., Int. Ed.* **2017**, *56*, 16047–16051.
- (47) Xu, W.; Zhu, S.; Liang, Y.; Cui, Z.; Yang, X.; Inoue, A.; Wang, H. A Highly Efficient Electrocatalyst Based on Amorphous Pd – Cu – S Material for Hydrogen Evolution Reaction. *J. Mater. Chem. A* **2017**, *5*, 18793–18800.
- (48) Cheng, T.; Wang, L.; Merinov, B. V.; Goddard, W. A. Explanation of Dramatic PH-Dependence of Hydrogen Binding on Noble Metal Electrode: Greatly Weakened Water Adsorption at High PH. *J. Am. Chem. Soc.* **2018**, *140*, 7787–7790.
- (49) Ledezma-yanez, I.; Wallace, W. D. Z.; Sebastián-pascual, P.; Climent, V.; Feliu, J. M.; Koper, M. T. M. Interfacial Water Reorganization as a PH-Dependent Descriptor of the Hydrogen Evolution Rate on Platinum Electrodes. *Nat. Energy* **2017**, *2*, 17031.
- (50) Liu, E.; Li, J.; Jiao, L.; Doan, H. T. T.; Liu, Z.; Zhao, Z.; Huang, Y.; Abraham, K. M.; Mukerjee, S.; Jia, Q. Unifying the Hydrogen Evolution and Oxidation Reactions Kinetics in Base by Identifying the Catalytic Roles of Hydroxyl-Water-Cation Adducts. *J. Am. Chem. Soc.* **2019**, *141*, 3232–3239.
- (51) Durst, J.; Simon, C.; Siebel, A.; Rheinlander, P. J.; Schuler, T.; Hanzlik, M.; Herranz, J.; Hasche, F.; Gasteiger, H. A. (Invited) Hydrogen Oxidation and Evolution Reaction (HOR/HER) on Pt Electrodes in Acid vs. Alkaline Electrolytes: Mechanism, Activity and Particle Size Effects. *ECS Trans.* **2014**, *64*, 1069–1080.
- (52) Sha, Y.; Yu, T. H.; Merinov, B. V.; Goddard, W. A. DFT Prediction of Oxygen Reduction Reaction on Palladium – Copper Alloy Surfaces. *ACS Catal.* **2014**, *4*, 1189–1197.
- (53) Xi, Z.; Li, J.; Su, D.; Muzzio, M.; Yu, C.; Li, Q.; Sun, S. Stabilizing CuPd Nanoparticles via CuPd Coupling to WO_{2.72}Na-norods in Electrochemical Oxidation of Formic Acid. *J. Am. Chem. Soc.* **2017**, *139*, 15191–15196.
- (54) Gunji, T.; Noh, S. H.; Tanabe, T.; Han, B.; Nien, C. Y.; Ohnsaka, T.; Matsumoto, F. Enhanced Electrocatalytic Activity of Carbon-Supported Ordered Intermetallic Palladium – Lead (Pd 3 Pb) Nanoparticles toward Electrooxidation of Formic Acid. *Chem. Mater.* **2017**, *29*, 2906–2913.
- (55) Hu, C.; Guo, Y.; Wang, J.; Yang, L.; Yang, Z.; Bai, Z.; Zhang, J.; Wang, K.; Jiang, K. Additive-Free Fabrication of Spherical Hollow Palladium/Copper Alloyed Nanostructures for Fuel Cell Application. *ACS Appl. Mater. Interfaces* **2012**, *4*, 4461–4464.
- (56) Yang, N.; Zhang, Z.; Chen, B.; Huang, Y.; Chen, J.; Lai, Z.; Chen, Y.; Sindoro, M.; Wang, A. L.; Cheng, H.; Fan, Z.; Liu, X.; Li, B.; Zong, Y.; Gu, L.; Zhang, H. Synthesis of Ultrathin PdCu Alloy Nanosheets Used as a Highly Efficient Electrocatalyst for Formic Acid Oxidation. *Adv. Mater.* **2017**, *29*, 1700769.
- (57) Wang, X.; Yang, J.; Yin, H.; Song, R.; Tang, Z. Raisin Bun”-Like Nanocomposites of Palladium Clusters and Porphyrin for Superior Formic Acid Oxidation. *Adv. Mater.* **2013**, *25*, 2728–2732.
- (58) Zhang, L.; Choi, S. Il; Tao, J.; Peng, H. C.; Xie, S.; Zhu, Y.; Xie, Z.; Xia, Y. Pd-Cu Bimetallic Tripods: A Mechanistic Understanding of the Synthesis and Their Enhanced Electrocatalytic Activity for Formic Acid Oxidation. *Adv. Funct. Mater.* **2014**, *24*, 7520–7529.